Materials Advances

ROYAL SOCIETY OF CHEMISTRY

PAPER

View Article Online
View Journal | View Issue

Cite this: *Mater. Adv.*, 2023, 4, 3551

High-performance Ruddlesden–Popper two-dimensional perovskite solar cells using integrated electron transport materials of tin oxide and indacenodithiophene†

Zhihai Liu,[a] Lei Wang,[b] Hao Zhao,[a] Yibin Wei,[c] Xiaoyin Xie*[d] and Ping Chen*[a]

Perovskite solar cells (PSCs) have been rapidly developed and exhibit comparable power conversion efficiency (PCE) to silicon solar cells. However, the stability of PSCs needs to be further enhanced to satisfy the requirement of commercialization. As a result, Ruddlesden–Popper (RP) type two-dimensional (2D) perovskites with high intrinsic stability have been intensively studied. In this work, we improved the performance of RP-type 2D PSCs using tin oxide (SnO_2) and indacenodithiophene (IDIC) as an integrated electron transport layer (ETL). Here, IDIC is used to tune the energy alignment and hydrophobicity of SnO_2, which further improves the electron transport properties and film quality of perovskite. With the deposition of 15 nm IDIC on SnO_2, the average PCE of the 2D PSCs was significantly improved from 11.7% to 14.8%, with simultaneously enhanced short-circuit current density and fill factor. The long-term stability of the studied 2D PSCs also improved with the PCE degradation significantly suppressed from 24.8% to 16.2% after a duration of 20 days. The best PSC with the integrated ETL of SnO_2/IDIC exhibited a high PCE of 15.2%, with stable power output and negligible hysteresis. Our results demonstrate a simple and effective method for improving the performance of RP PSCs.

Received 9th May 2023,
Accepted 7th July 2023

DOI: 10.1039/d3ma00221g

rsc.li/materials-advances

1. Introduction

In recent years, organo-metal halide perovskite solar cells (PSCs) have been intensively investigated owing to their unique advantages of high power-conversion-efficiency (PCE), convenient material source, and simple solution processability.[1–4] Since Kojima *et al.* first applied perovskite in solar cells in 2009,[5] PSCs have been rapidly developed, with PCE significantly improving from 3.8% to 25.7%.[6] As a result, PSCs are believed as one of the next-generation photovoltaics, indicating great potential for commercial application. However, PSCs suffer a serious problem of poor stability because conventional $MAPbX_3$ (MA = CH_3NH_3, X = Cl, Br, or I) perovskites can be hydrated by moisture in the air and gradually decompose into PbI_2.[7,8] To overcome this problem, several strategies have been investigated, such as improving the film quality of perovskite, adopting moisture-resistant charge transport layers, and developing effective encapsulating technologies.[9–11] Recently, low-dimensional perovskite materials have been developed for replacing $MAPbX_3$ in PSCs, which could improve the stability of PSCs.[12–19] For example, two-dimensional perovskites, specifically Ruddlesden–Popper (RP) type, have been widely used as absorbers in PSCs, which own sufficient light absorption and tunable energy bands.[20] PSCs using $(BA)_2(MA)_{n-1}Pb_nI_{3n+1}$ (n is an integer, BA is $CH_3(CH_2)_3NH_3$) RP perovskites showed enhanced stability compared to conventional $MAPbX_3$ based PSCs.[21–25]

PSCs are usually fabricated with a layer-by-layer structure, in which perovskite absorbers are sandwiched between the charge transport layers. A high-quality perovskite film with uniform morphology is a basic requirement for fabricating highly efficient PSCs with good stability.[26] Although techniques such as on-step or two-step spin coating, hot casting, and anti-solvent dropping could improve the film quality of perovskites, some defects could still be found in the films.[26–28] This was mainly induced by the decomposition and evaporation of MAI under high temperatures, leaving vacancies in the perovskite structure.[29] As a result, passivating these defects can improve

[a] *School of Physics and Electronic Information, Yantai University, Yantai, 264005, China. E-mail: chenping@ytu.edu.cn*
[b] *School of Artificial Intelligence, Beijing Technology and Business University, Beijing, 100048, China*
[c] *State Key Laboratory of High-efficiency Utilisation of Coal and Green Chemical Engineering, Ningxia University, Yinchuan 750021, China*
[d] *School of Chemistry and Chemical Technology, Hubei Polytechnic University, Huangshi 435003, China. E-mail: xyxie@hbpu.edu.cn*

† Electronic supplementary information (ESI) available: Additional figures and tables. See DOI: https://doi.org/10.1039/d3ma00221g

the opto-electronic properties of the perovskite films, which is beneficial for boosting the performance of PSCs.[30] For standard n–i–p structured PSCs, planar or mesoporous TiO_2 is usually used as the electron transport layer (ETL). However, processing TiO_2 requires a high temperature of about 500 °C,[3] which is a restriction to mass production. To solve this problem, researchers developed some other n-type materials with suitable energy alignment and lower processing temperatures. For example, C_{60}, phenyl-C61-butyric acid methyl ester (PCBM), ZnO, and SnO_2 have been reported as the ETLs in PSCs, which can be prepared under a low temperature of 80–200 °C.[31–34] Among them, SnO_2 showed a deeper conduction band (CB) and higher electron mobility ($\mu_{electron}$, $\sim 1.9 \times 10^{-3}$ cm^2 V^{-1} s^{-1}) than TiO_2, which resulted in a better performance for $(FAPbI_3)_x(MAPbBr_3)_{1-x}$-based PSCs.[34] Different from PCBM, indacenodithiophene (IDIC) is an organic π-conjugated non-fullerene n-type acceptor with a higher $\mu_{electron}$ ($\sim 1.1 \times 10^{-3}$ cm^2 V^{-1} s^{-1}),[35] which is a good candidate as electron transport material in PSCs. Zhang *et al.* used IDIC to replace TiO_2 in standard n–i–p PSCs, which improved the crystallization of the perovskite ($MAPbI_3$) film. Based on this technique, the PSCs showed an improved PCE of 19.1% with enhanced stability.[36] Lin *et al.* found that IDIC could effectively passivate surface defects of perovskite ($MAPbI_3$), which resulted in a high PCE of 19.4% for inverted p–i–n PSCs.[30] Our previous study demonstrated that IDIC could efficiently passivate defects in RP $(BA)_2(MA)_3Pb_4I_{13}$ perovskite, which further improved the PCE of the PSCs from 10.2% to 12.8%.[37]

In this study, we developed an integrated ETL of SnO_2/IDIC for improving the performance of n–i–p structured 2D RP PSCs. Inserting IDIC between SnO_2 and perovskite could tune the energy alignment and improve the perovskite quality. The improved energy alignment is beneficial for electron transport from perovskite to electrode. The hydrophobic surface of IDIC could enhance the crystallization of the $(BA)_2(MA)_3Pb_4I_{13}$ perovskite and passivate the defects formed in it. As a result, PSCs using SnO_2/IDIC showed an average PCE of 14.8%, which is significantly higher than that (11.7%) of PSCs using bare SnO_2. Open-circuit voltage (V_{oc}), short-circuit current density (J_{sc}), and the fill factor (FF) of the devices were improved simultaneously. Furthermore, the long-term stability of the PSCs was enhanced upon using SnO_2/IDIC, with the PCE degradation significantly suppressed from 26.8% to 16.2% after a measurement of 20 days. The best RP PSC using SnO_2/IDIC exhibited a high PCE of 15.2% with stable power output and negligible hysteresis. Our results demonstrate the superior performance of 2D PSCs upon using hybrid SnO_2/IDIC as the ETL.

2. Experimental section

2.1 Device fabrication

IDIC, PCBM, and methylammonium iodide (MAI) were purchased from 1-Materials Inc. (Canada), Nano-C Inc. (USA), and Advanced Election Technology Co., Ltd (China). Butylammonium iodide (BAI), PbI_2, bis(trifluoromethane) sulfonamide lithium salt, 4-*tert*-butylpyridine (*t*BP), 2-methoxyethanol, acetonitrile, *N*,*N*-dimethylformamide (DMF), dimethyl sulfoxide (DMSO), and chlorobenzene were purchased from Sigma–Aldrich (USA). The SnO_2 colloidal dispersion (15% in water) and 2,2′,7,7′-tetrakis-(*N*,*N*-di-*p*-methoxyphenylamine)-9,9′-spirobifluorene (spiro-OMeTAD) were purchased from Alfa Aesar (USA) and Xi'an Polymer Light Technology Corp. (China),

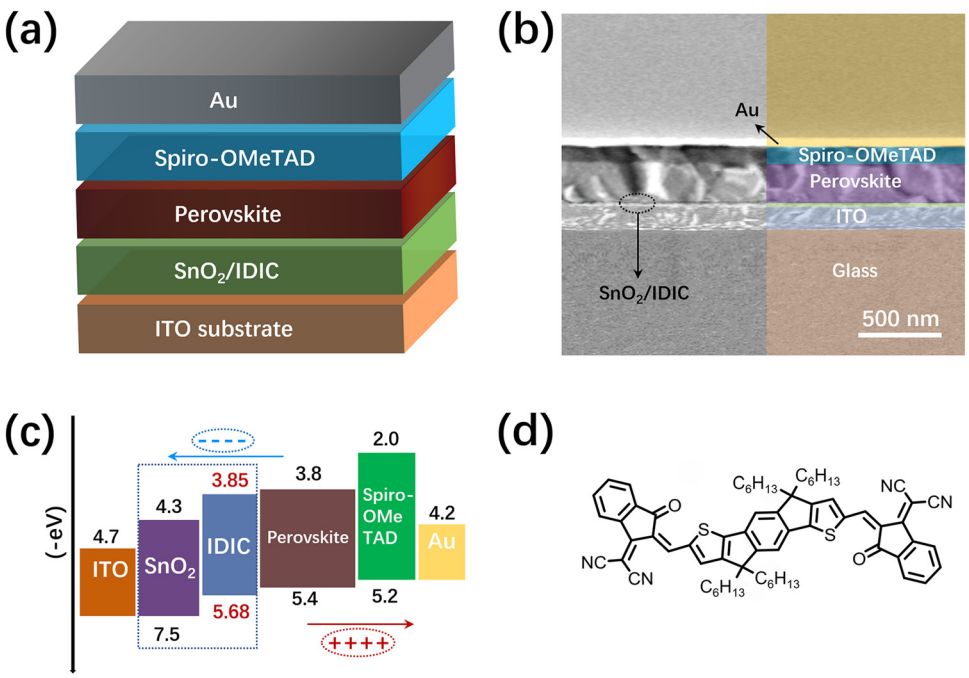

Fig. 1 (a) Schematic structure of the RP PSCs; (b) cross-sectional SEM image of a PSC; (c) energy alignment of the functional layers involved in the PSCs; (d) molecular structure of IDIC.

respectively. The perovskite precursor was prepared by dissolving BAI, MAI, and PbI_2 (molar ratio = 2 : 3 : 4) in a mix-solvent of DMF and DMSO (85 : 15 by volume) at a total concentration of 40 wt%. The spiro-OMeTAD solution was prepared by dissolving 75 mg spiro-OMeTAD, 28 μL *t*BP, and 18 μL mixture of lithium salt (520 mg in 1 mL acetonitrile) in 1 mL chlorobenzene. The SnO_2 precursor was prepared by diluting the SnO_2 dispersion to 2.67% in water. As shown in Fig. 1(a), the RP PSCs were fabricated on pre-patterned indium-tin oxide (ITO)-coated substrates with a structure of glass/ITO/SnO_2/IDIC/perovskite/spiro-OMeTAD/Au. First, the SnO_2 precursor was spin coated onto the ITO glasses at 4000 rpm for 45 s. The samples were then thermally annealed at 150 °C for 30 min. The IDIC solution (in chlorobenzene at 10 mg mL^{-1}) was spin coated onto the SnO_2 layers at 1000, 1500, or 2000 rpm, followed by thermal annealing at 100 °C in a N_2 filled glove box. For control devices, the operation of coating IDIC was skipped. After that, the perovskite precursor was spin coated onto the ETLs at 4000 rpm for 45 s. The RP $(BA)_2(MA)_3Pb_4I_{13}$ perovskite films were then formed after being heated at 100 °C for 10 min. Subsequently, the spiro-OMeTAD solution was spin coated onto the perovskite layers, followed by thermal annealing at 80 °C. Finally, the Au anodes of about 100 nm were thermally evaporated onto the spiro-OMeTAD layers under a low pressure of 10^{-4} Pa. The effective working area of the PSCs is 0.1 cm^2, which is defined by a shadow mask.

2.2 Characterization

The ultraviolet-visible (UV-vis) absorption spectra were characterized using a spectrophotometer (PerkinElmer Lambda 750, USA). The X-ray diffraction (XRD) patterns of the perovskite films were obtained using an X-ray diffractometer (Panalytical, Netherlands). Cross-sectional images of the PSCs and top-view images of the perovskite surfaces were acquired using an SU8020 scanning electron microscope (SEM, Hitachi, Japan) operated at the acceleration voltage of 8 kV. Photoluminescence (PL) spectra were measured using a spectrometer (FLS920, Edinburgh Instruments, UK). The energy levels of IDIC were measured using an ultraviolet photoelectron spectroscope (UPS) with the incident light energy (He I) of 21.22 eV. The electrochemical impedance spectroscopy (EIS) of the PSCs were performed using an electrochemical workstation (Bio-Logic, France). The current density–voltage (*J*–*V*) characteristics of the devices were measured at an irradiation intensity of 100 mW cm^{-2} (AM1.5). The incident photon-to-current efficiency (IPCE) was measured using a solar cell IPCE measurement system (Solar Cell Scan 100, Zolix, China).

3. Results and discussion

The cross-sectional SEM image of the PSCs is shown in Fig. 1(b), which reveals a typical layer-by-layer structure. From the SEM image, the thicknesses of the perovskite and spiro-OMeTAD layers are about 400 and 220 nm, respectively. Fig. 1(c) shows the energy alignment in the PSCs, which indicates the charge transport progress in the PSCs. The generated electrons will transport through ETL to the left ITO cathode, and the holes will transport through spiro-OMeTAD to the Au anode on the right side. The molecular structure of IDIC is shown in Fig. 1(d), which contains Lewis base groups (C═O and C≡N) at the ends of the structure. As indicated from previous studies,[38,39] conduction band (CB) of SnO_2 is −4.3 eV, which is much lower than the lowest unoccupied molecular orbital (LUMO) level (−3.8 eV) of $(BA)_2(MA)_3Pb_4I_{13}$ perovskite. As shown in Fig. 2(a) and (b), IDIC is an n-type semiconductor with a highest occupied molecular orbital level of −5.68 eV. The LUMO level of IDIC is calculated as −3.85 eV, which lies between the CB of SnO_2 and the LUMO level of perovskite. Such an energy alignment is beneficial for electron extraction from the perovskite absorber, which will be discussed later.

The *J*–*V* characteristics of the RP PSCs are shown in Fig. 3(a), with the extracted device parameters summarized in Table 1. The control PSCs using bare SnO_2 as ETL showed an average PCE of 11.7%, with V_{oc} of 1.03 V, J_{sc} of 17.9 mA cm^{-2}, and FF of 63.5%. These are typical values for $(BA)_2(MA)_3Pb_4I_{13}$ based PSCs existing in previous studies.[19–25] We controlled the thickness of IDIC by altering the rotating speed of the spin coating operation. When coating IDIC at 1000 rpm onto SnO_2, the PCE of the PSCs increased to 13.2% with simultaneously improved V_{oc}, J_{sc}, and FF. When coating IDIC at 1500 rpm, a maximal average PCE of 14.8% was obtained for the PSCs, with a high V_{oc} of 1.05 V, J_{sc} of 19.3 mA cm^{-2}, and FF of 72.8%. As shown from the

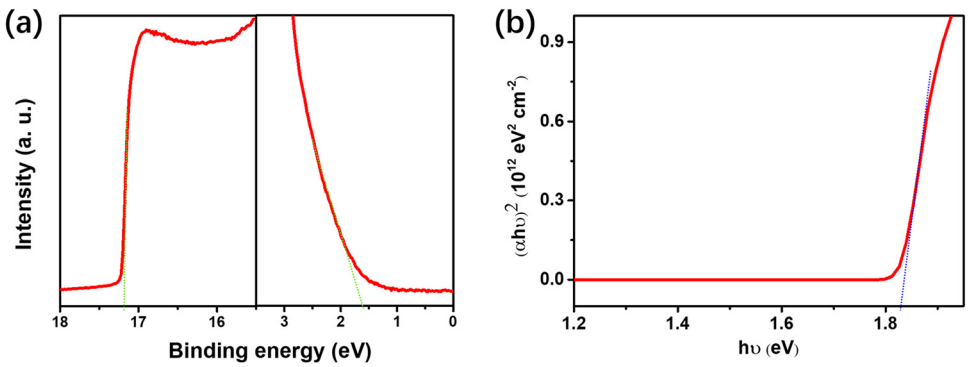

Fig. 2 UPS spectrum (a) and absorption coefficient as a function of photon energy (b) of the IDIC film.

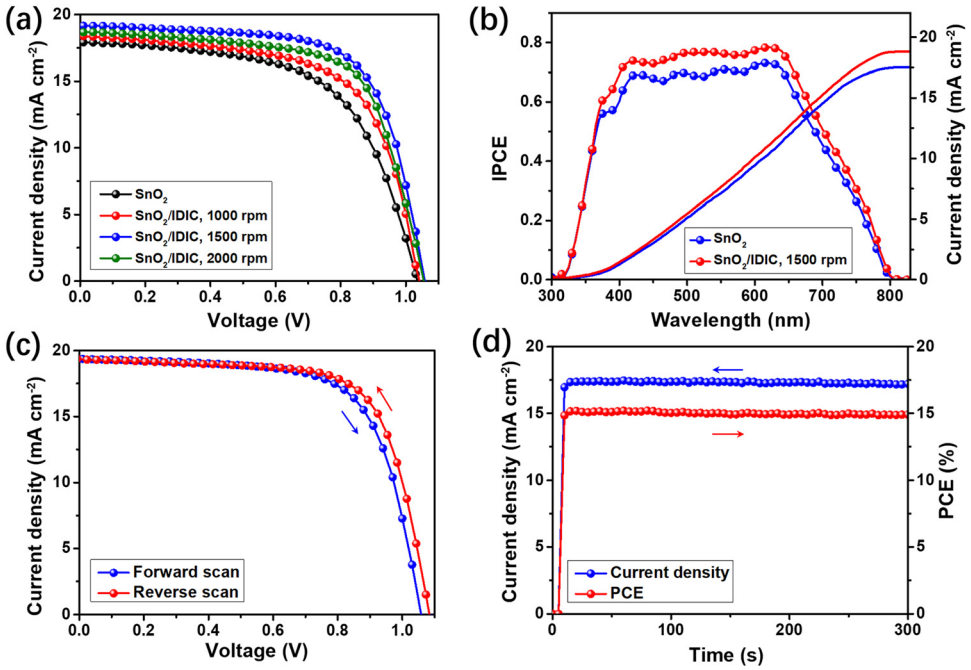

Fig. 3 (a) J–V characteristics of the RP PSCs using different ETLs of bare SnO_2 and SnO_2/IDIC, with IDIC films spin-coated using rotating speeds of 1000, 1500, or 2000 rpm; (b) IPCE spectra of the PSCs using ETLs of SnO_2 and SnO_2/IDIC with IDIC spin-coated from a speed of 1500 rpm; (c) forward and reverse J–V characteristics of the best-performing RP PSC with SnO_2/IDIC; (d) current density and PCE as a function of time for the best-performing 2D PSC, under a forward bias of 0.86 V.

Table 1 Device parameters of the RP PSCs based on different ETLs of bare SnO_2 and SnO_2/IDIC, in which IDIC was spin coated from rotating speeds of 1000, 1500, or 2000 rpm

Device configuration	V_{oc} (V)	J_{sc} (mA cm^{-2})	FF (%)	Average PCE (%)	Best PCE (%)
Bare SnO_2	1.03 ± 0.01	17.9 ± 0.3	63.5 ± 1.3	11.7 ± 0.3	12.1
SnO_2 with IDIC, 1000 rpm	1.04 ± 0.01	18.5 ± 0.2	68.6 ± 1.2	13.2 ± 0.2	13.5
SnO_2 with IDIC, 1500 rpm	1.05 ± 0.01	19.3 ± 0.3	72.8 ± 1.3	14.8 ± 0.3	15.2
SnO_2 with IDIC, 2000 rpm	1.05 ± 0.01	18.7 ± 0.3	70.5 ± 1.2	13.9 ± 0.3	14.3

AFM image in Fig. S1 (ESI†), the thickness of the IDIC film processed at 1500 rpm is about 15 nm, which is optimal for boosting the performance of the RP PSCs. The statistical PCEs with standard deviations for the control and 15 nm IDIC-based PSCs are shown in Fig. S2 (ESI†), which indicate a stable performance for each batch of PSCs. Further decreasing the thickness of IDIC (increasing rotating speed) induced a lower performance for the PSCs, with a degraded PCE of 13.9%. As shown in Fig. 3(b), we compared the IPCE spectra of the PSCs using bare SnO_2 and SnO_2/IDIC (under a coating speed of 1500 rpm) as the ETLs. From the IPCE spectra, the calculated J_{sc} for the control and best groups are 17.5 and 18.8 mA cm^{-2}, respectively. Compared with the J–V characteristics, the difference between the measured and calculated J_{sc} is less than 2.6%, indicating the accurate J–V measurements. The forward and reverse scanning J–V characteristics of the best PSC using SnO_2/IDIC are shown in Fig. 3(c), which indicates a small hysteresis for the PSC. By reverse scan, the PCE slightly increased to 15.5%, which was induced by the increased V_{oc} (1.08 V) and FF (73.6%). Compared with previous studies,[24–26] excellent PCEs of 15.2–15.5% were obtained for $(BA)_2(MA)_3Pb_4I_{13}$ based PSCs. Fig. 3(d) shows the steady-state power outputs of the best-performing device over a duration of 300 s. The current density could stabilize at about 17.5 mA cm^{-2} under a bias of 0.86 V, leading to a PCE range of 14.8–15.0%.

Fig. S3(a) (ESI†) shows the SEM image of the prepared SnO_2 film on glass, which indicates a rough surface morphology. From Fig. S2(b) (ESI†), the surface of IDIC/SnO_2 appears much smoother, which is beneficial for forming ohmic contact with perovskite. Moreover, as shown in Fig. S3(c) and (d) (ESI†), the contact angles of SnO_2 and SnO_2/IDIC are 32° and 78°, respectively. This indicates a more hydrophobic property of the surface upon coating IDIC, which may affect the crystallization process of the upper perovskite.[40] The performance of the PSCs is significantly affected by the quality of the perovskite films, which determines light absorption and charge generation.[26] Here, we characterized the quality of perovskite films formed on underlayers of bare SnO_2 and SnO_2/IDIC using SEM, UV-vis absorption, and XRD measurements. Fig. 4(a) shows the SEM image of the perovskite film formed on bare SnO_2 with some

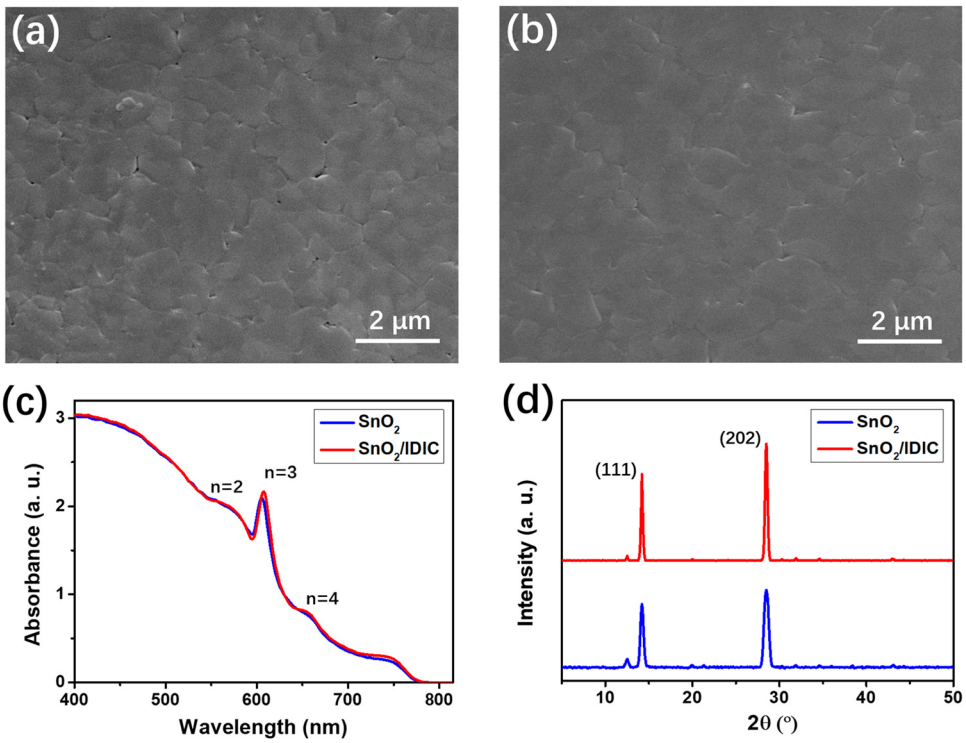

Fig. 4 SEM image of the $(BA)_2(MA)_3Pb_4I_{13}$ perovskite films formed on bare SnO_2 (a) and SnO_2/IDIC (b); UV-vis absorption spectra (c), and XRD patterns of the perovskite films formed on bare SnO_2 and SnO_2/IDIC.

pinholes observed on the surface. As shown in Fig. 4(b), the perovskite formed on SnO_2/IDIC exhibited a smooth and uniform surface morphology without clear pinholes. The perovskite grains were enlarged from 0.5–1.5 μm to 1.2–2.5 μm, indicating the reduced boundaries of the perovskite film formed on the underlying SnO_2/IDIC. Fig. 4(c) presents the UV-vis absorption spectra for the two perovskite films, which showed a broad absorption range of 400–800 nm. The specific absorption peak of $(BA)_2(MA)_3Pb_4I_{13}$ perovskite on SnO_2/IDIC is 611 nm, which indicated a slight red shift to that of perovskite formed on SnO_2. From the absorption spectra, a small amount of other 2D perovskite phases (*e.g.* n = 2 and 4) may be formed during the preparation of $(BA)_2(MA)_3Pb_4I_{13}$ (n = 3). The XRD patterns for the two perovskite films are shown in Fig. 4(d), in which two dominant peaks at 14.2° and 28.5° can be observed. From previous studies, the two peaks corresponded to the crystallographic (111) and (202) planes of the $(BA)_2(MA)_3Pb_4I_{13}$ perovskite.[22,37] By using SnO_2/IDIC as the underlying ETL, these characteristic peaks became stronger and sharper, indicating the enhanced crystallinity of the perovskite film. Moreover, the peaks at about 12.5° correspond to the (001) lattice planes of hexagonal PbI_2, which was reduced upon using IDIC. This indicates the promoted crystallization of perovskite formed on SnO_2/IDIC substrates. The SEM, UV-vis absorption, and XRD results demonstrate the improved quality of the perovskite film prepared on SnO_2/IDIC, which can be explained by the hydrophobic property of the underlayer. Previous studies indicate that a hydrophobic surface could suppress the nucleation of perovskite in small cavities at the initial stage of spin-coating.[40,41] Then, larger spaces between the perovskite nuclei would be induced due to the increased Gibbs free-energy barrier for nucleation. Moreover, a hydrophobic surface could reduce the anchoring effect of the precursor solution, which facilitates the migration of perovskite grains.[41] As a result, using hydrophobic underlying SnO_2/IDIC improved the processes of both nucleation and grain growth for the perovskite film, leading to improved crystallization.

To analyze the mechanism for performance improvement of the PSCs, we measured *J–V* characteristics of the electron-only space-charge-limited current (SCLC) devices using a structure of glass/ETL/perovskite/PCBM/Ag, in which ETL used SnO_2 or SnO_2/IDIC. As shown in Fig. 5(a), the current density increases linearly with voltage at the low voltage range (left part), indicating the ohmic response.[42] At the range of middle voltage, the current density increases much more rapidly with voltage, which suggests the trap-filled limit. The voltage between the ohmic and trap-filled ranges is defined as the trap-filled limit voltage (V_{TFL}), which is highly related to the number of trap states. The trap density (n_{trap}) can be calculated using eqn (1):[43]

$$V_{TFL} = \frac{en_{trap}L^2}{2\varepsilon_0\varepsilon} \quad (1)$$

where L is the thickness of the perovskite film, ε_0 is the vacuum permittivity, ε is the relative dielectric constant of perovskite, and e is the elementary charge. From Fig. 5(a), the V_{TFL} of the devices using bare SnO_2 is 0.53 V, which is much higher than that (0.26 V) of SnO_2/IDIC-based devices. Accordingly, the calculated n_{trap} is reduced from 5.9×10^{15} to 2.8×10^{15} cm^{-3}

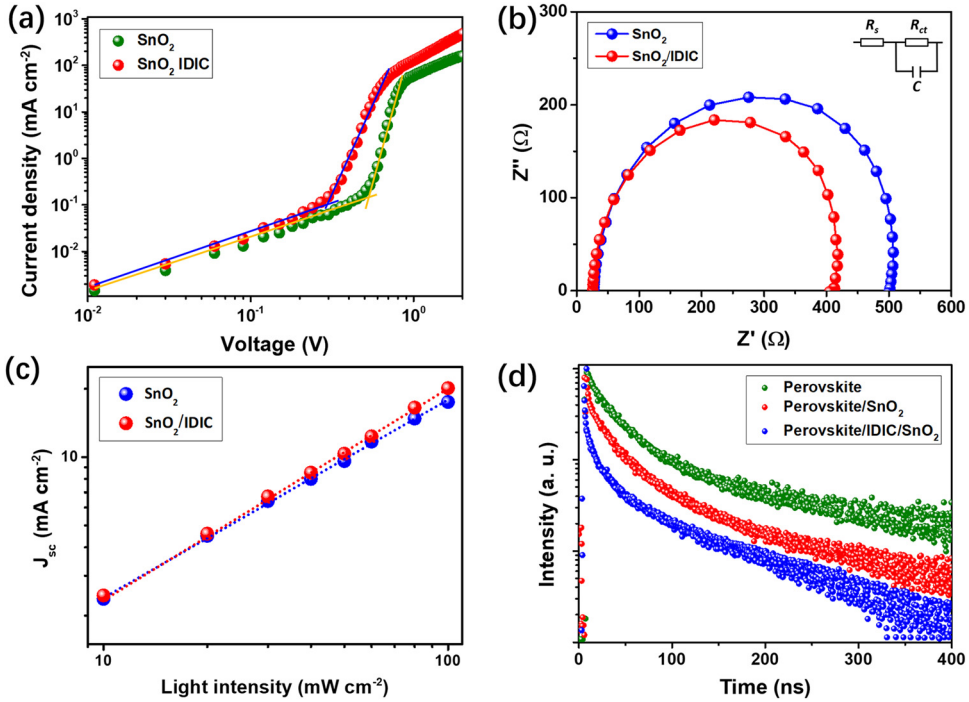

Fig. 5 (a) J–V characteristics of the electron-only SCLC devices based on the structure of glass/ETL/perovskite/PCBM/Ag (ETL is SnO_2 or SnO_2/IDIC); (b) Nyquist plots of PSCs using bare SnO_2 and SnO_2/IDIC as the ETLs with inset showing the equivalent circuit; (c) light intensity dependence of J_{sc} for PSCs using bare SnO_2 and SnO_2/IDIC as the ETLs; (d) TRPL spectra of bare perovskite, perovskite on SnO_2, and perovskite on SnO_2/IDIC.

upon using SnO_2/IDIC as the ETL. The lower n_{trap} can be attributed to the improved quality of perovskite film and defect passivation of IDIC. As indicated in Fig. 4, a well-crystalized perovskite film has fewer intrinsic defects, which results in a lower n_{trap}. On the other hand, the IDIC contains Lewis base groups (C═O and C≡N) at the branches of the structure, which could form coordinate bonds with the under-coordinated Pb atoms of the perovskite.[30] As a result, using IDIC between SnO_2 and perovskite could effectively passivate the vacancy-induced defects of RP perovskite, which further reduced the number of carrier traps.[37] Moreover, $\mu_{electron}$ of the devices can be calculated from the high voltage Child region, using the Mott–Gurney law:[25]

$$J = \frac{9}{8}\varepsilon\varepsilon_0\mu\frac{V^2}{L^3} \quad (2)$$

in which the calculated $\mu_{electron}$ of the SnO_2 and SnO_2/IDIC based devices are 5.7 × 10^{-4} and 8.5 × 10^{-4} cm^2 V^{-1} s^{-1}, respectively. To characterize the charge transport property, we measured the EIS spectra of the PSCs using different ETLs in dark conditions. As shown in Fig. 5(b), the EIS spectra can be fitted using the equivalent circuit shown inset, which consists of a series resistance (R_s), a charge transfer resistance (R_{ct}), and a capacitor (C).[44] In PSCs, R_s is usually determined by the interfacial connections between different functional layers, while R_{ct} reflects the charge transfer process from perovskite absorber to electrodes. From the fitted parameters, R_{ct} of the PSCs using SnO_2/IDIC is 352 Ω, which is lower than that (467 Ω) of devices using bare SnO_2. This indicates the improved charge transport property of PSCs using SnO_2/IDIC as ETL. We also analyzed the charge recombination property of the PSCs using different ETLs by measuring the relation between J_{sc} and incident light density. As shown in Fig. 5(c), the fitted slope of the PSCs using bare SnO_2 as ETL is 0.93, which is lower than that (0.98) of the PSCs using SnO_2/IDIC. The increased slope indicates the suppressed bi-molecular charge recombination in the PSCs upon using SnO_2/IDIC, which occurs at the interface of perovskite and charge transport layers.[45] From the dependence of V_{oc} and light density shown in Fig. S4 (ESI†), the control PSCs showed a slope of 1.51kT/e, where k is the Boltzmann constant, and T is the absolute temperature. By using IDIC, the slope was decreased to 1.33kT/e, which indicates the reduced trap-assisted recombination in the PSCs.[46] From the dark J–V characteristics shown in Fig. S5 (ESI†), the left part of J under the reverse bias became lower for the PSCs using IDIC. This indicates a weaker leakage current upon using IDIC in PSCs, consistent with the suppressed charge recombination. To demonstrate the electron extraction property of the ETLs, we measured the time-resolved PL (TRPL) spectra for the films of bare perovskite, perovskite on SnO_2, and perovskite on SnO_2/IDIC. As shown in Fig. 5(d), the PL lifetime was reduced by using SnO_2 or SnO_2/IDIC as the underlayer, which was induced by the quenching effect of excitons. With bi-exponential fitting to the spectra, using SnO_2 could decrease the PL lifetime for perovskite from 332 to 125 ns. Using SnO_2/IDIC further decreased the PL lifetime to 73 ns, indicating an enhanced quenching effect for excitons.[32] The TRPL result demonstrates the improved electron extraction from perovskite

upon using SnO_2/IDIC, which can be explained by the improved energy alignment. As shown in Fig. 2(c), the LUMO level of IDIC (−3.85 eV) could more efficiently transport the generated electrons from the perovskite absorber. From the above analysis, the performance of the PSCs can be attributed to the improved energy alignment, better film quality of perovskite, and defect passivation upon using SnO_2/IDIC as the ETL.

In addition, we compared the stability performance of the PSCs using bare SnO_2 and SnO_2/IDIC as the ETLs by testing the samples for 20 days. The unencapsulated samples were stored in dark conditions at room temperature (25 °C) under a relative humidity of 30–40%. As shown in Fig. S6 (ESI†), the final PCE of the control SnO_2-based PSCs retained only 8.8%, corresponding to a PCE degradation of 24.8% (original PCE was 11.7%). For PSCs using SnO_2/IDIC, the PCE was 12.4% after 20 days, indicating a weaker PCE degradation of 16.2% (original PCE was 14.8%). As a result, the PSCs using SnO_2/IDIC as the ETL showed enhanced long-term stability with significantly suppressed PCE degradation. The improved stability can be explained by the higher hydrophobic property of IDIC and the better quality of the perovskite film. This is because the hydrophobic IDIC could efficiently block moisture from the air to the device, suppressing the hydrated decomposition of perovskite. Moreover, a well-crystalized perovskite film usually exhibits higher intrinsic stability,[8,47] which is induced by the insertion of IDIC. Therefore, using integrated ETL of SnO_2/IDIC can simultaneously improve the PCE and stability of the RP PSCs.

4. Conclusions

In summary, we simultaneously improved the PCE and stability of the RP PSCs by developing an integrated ETL of SnO_2/IDIC. By inserting IDIC between perovskite and SnO_2, the energy alignment of the PSCs and hydrophobicity of the underlayer were tuned, which improved the charge transport and perovskite formation. Consequently, the PSCs using SnO_2/IDIC exhibited an average PCE of 14.8%, which is significantly higher than that (11.7%) of PSCs using bare SnO_2. The results of light absorption, SEM, and XRD measurements demonstrated the improved perovskite quality upon using SnO_2/IDIC as the underlying ETL. The SCLC model, EIS, and TRPL results suggested improved charge transport and suppressed charge recombination in the PSCs. The long-term stability of PSCs was largely enhanced, with PCE degradation significantly reduced from 24.8% to 16.2% after 20 days. The best sample using SnO_2/IDIC exhibited an excellent PCE of 15.2% with stable power output and negligible hysteresis. Our results demonstrate that using integrated ETL of SnO_2/IDIC is a simple and effective way to boost the performance of RP PSCs.

Conflicts of interest

There are no conflicts to declare.

Acknowledgements

This work was supported by the Developing Plan for College Youth Innovative Group of 2022 (funded by the National Natural Science Foundation of China, No. 11874318) and Hubei Polytechnic University Talent Introduction Foundation (No. 51871067).

References

1 W. S. Yang, B.-W. Park, E. H. Jung, N. J. Jeon, Y. C. Kim, D. U. Lee, S. S. Shin, J. Seo, E. K. Kim, J. H. Noh and S. I. Seok, *Science*, 2017, **356**, 1376–1379.
2 M. M. Lee, J. Teuscher, T. Miyasaka, T. N. Murakami and H. J. Snaith, *Science*, 2012, **338**, 643–647.
3 J. Y. Kim, J.-W. Lee, H. S. Jung, H. Shin and N.-G. Park, *Chem. Rev.*, 2020, **120**, 7867–7918.
4 Z. Guo, A. K. Jena, G. M. Kim and T. Miyasaka, *Energy Environ. Sci.*, 2022, **15**, 3171–3222.
5 A. Kojima, K. Teshima, Y. Shirai and T. Miyasaka, *J. Am. Chem. Soc.*, 2009, **131**, 6050–6051.
6 NREL Best Research-Cell Efficiency Chart (Photovoltaic Research). Available online: **https://www.nrel.gov/pv/cell-efficiency.html** (accessed on 12 January 2023).
7 R. Wang, M. Mujahid, Y. Duan, Z.-K. Wang, J. Xue and Y. Yang, *Adv. Funct. Mater.*, 2019, **29**, 1808843.
8 L. Duan and A. Uddin, *Mater. Chem. Front.*, 2022, **6**, 400–417.
9 S. Ma, S. Pang, H. Dong, X. Xie, G. Liu, P. Dong, D. Liu, W. Zhu, H. Xi, D. Chen, C. Zhang and Y. Hao, *Polymers*, 2022, **14**, 343.
10 K. Lee, H. Yu, J. W. Lee, J. Oh, S. Bae, S. K. Kim and J. Jang, *J. Mater. Chem. C*, 2018, **6**, 6250–6256.
11 J. Li, R. Xia, W. Qi, X. Zhou, J. Cheng, Y. Chen, G. Hou, Y. Ding, Y. Li, Y. Zhao and X. Zhang, *J. Power Sources*, 2021, **485**, 229313.
12 P. Liu, N. Han, W. Wang, R. Ran, W. Zhou and Z. Shao, *Adv. Mater.*, 2021, **33**, 2002582.
13 Y. Zhao, H. Xiang, R. Ran, W. Zhou, W. Wang and Z. Shao, *J. Energy Chem.*, 2023, **83**, 189–208.
14 H. Xiang, P. Liu, R. Ran, W. Wang, W. Zhou and Z. Shao, *Renewable Sustainable Energy Rev.*, 2022, **166**, 112614.
15 L. Song, *Mater. Rep.: Energy*, 2022, **2**, 100171.
16 H. Xiang, P. Liu, W. Wang, R. Ran, W. Zhou and Z. Shao, *J. Mater. Sci. Technol.*, 2022, **113**, 138–146.
17 W. Shen, Y. Dong, F. Huang, Y.-B. Cheng and J. Zhong, *Rep. Energy*, 2021, **1**, 100060.
18 P. Li, X. Liu, Y. Zhang, C. Liang, G. Chen, F. Li, M. Su, G. Xing, X. Tao and Y. Song, *Angew. Chem., Int. Ed.*, 2020, **59**, 6909–6914.
19 L. Chao, T. Niu, Y. Xia, X. Ran, Y. Chen and W. Huang, *J. Phys. Chem. Lett.*, 2019, **10**, 1173–1179.
20 J. Shi, Y. Gao, X. Gao, Y. Zhang, J. Zhang, X. Jing and M. Shao, *Adv. Mater.*, 2019, **31**, 1901673.
21 H. Tsai, W. Nie, J.-C. Blancon, C. C. Stoumpos, R. Asadpour, B. Harutyunyan, A. J. Neukirch, R. Verduzco, J. J. Crochet,

S. Tretiak, L. Pedesseau, J. Even, M. A. Alam, G. Gupta, J. Lou, P. M. Ajayan, M. J. Bedzyk, M. G. Kanatzidis and A. D. Mohite, *Nature*, 2016, **536**, 312–316.

22 D. H. Cao, C. C. Stoumpos, O. K. Farha, J. T. Hupp and M. G. Kanatzidis, *J. Am. Chem. Soc.*, 2015, **137**, 7843–7850.

23 R. Liu, Y. Yu, T. Hu, F. Zhang, C. Liu, H. Hou, M. Zhang, X. Chen and H. Yu, *J. Power Sources*, 2021, **512**, 230452.

24 H. Li, X. Wang, T. Zhang, X. Gong, Q. Sun, H. Pan, Y. Shen, S. Ahmad and M. Wang, *Adv. Funct. Mater.*, 2019, **29**, 1903293.

25 Z. Liu, L. Wang and X. Xie, *J. Mater. Chem. C*, 2020, **8**, 11882–11889.

26 M. Qin, P. F. Chan and X. Lu, *Adv. Mater.*, 2021, **33**, 2105290.

27 Y. Niu, D. He, Z. Zhang, J. Zhu, T. Gavin, P. Falaras and L. Hu, *J. Energy Chem.*, 2022, **68**, 12–18.

28 S.-G. Kim, J.-H. Kim, P. Ramming, Y. Zhong, K. Schöz, S. J. Kwon, S. Huettner, F. Panzer and N.-G. Park, *Nat. Commun.*, 2021, **12**, 1554.

29 C. Li, A. Guerrero, S. Huettner and J. Bisquert, *Nat. Commun.*, 2018, **9**, 5113.

30 Y. Lin, L. Shen, J. Dai, Y. Deng, Y. Wu, Y. Bai, X. Zheng, J. Wang, Y. Fang, H. Wei, W. Ma, X. C. Zeng, X. Zhan and J. Huang, *Adv. Mater.*, 2017, **29**, 1604545.

31 C. Ji, C. Liang, H. Zhang, M. Sun, F. Sun, Q. Song, X. Zhang, D. Li, F. You and Z. He, *Org. Electron.*, 2018, **63**, 276–282.

32 G. Liu, X. Xie, Z. Liu, G. Cheng and E.-C. Lee, *Nanoscale*, 2018, **10**, 11043–11051.

33 P. Zhang, J. Wu, T. Zhang, Y. Wang, D. Liu, H. Chen, L. Ji, C. Liu, W. Ahmad, Z. D. Chen and S. Li, *Adv. Mater.*, 2018, **30**, 1703737.

34 Q. Jiang, L. Zhang, H. Wang, X. Yang, J. Meng, H. Liu, Z. Yin, J. Wu, X. Zhang and J. You, *Nat. Energy*, 2017, **2**, 16177.

35 Y. Lin, Q. He, F. Zhao, L. Huo, J. Mai, X. Lu, C.-J. Su, T. Li, J. Wang, J. Zhu, Y. Sun, C. Wang and X. Zhan, *J. Am. Chem. Soc.*, 2016, **138**, 2973–2976.

36 M. Zhang, J. Zhu, K. Liu, G. Zheng, G. Zhao, L. Li, Y. Meng, T. Guo, H. Zhou and X. Zhan, *J. Mater. Chem. A*, 2017, **5**, 24820–24825.

37 Z. Liu and E.-C. Lee, *Sustainable Energy Fuels*, 2021, **5**, 2354–2361.

38 Q. Jiang, X. Zhang and J. You, *Small*, 2018, **14**, 1801154.

39 C. Xu, Z. Liu, Q. Sun and E.-C. Lee, *Sol. Energy*, 2021, **214**, 280–287.

40 M. Hu, C. Bi, Y. Yuan, Y. Bai and J. Huang, *Adv. Sci.*, 2016, **3**, 1500301.

41 Z. Liu, L. Wang, C. Xu, X. Xie and Y. Zhang, *ACS Appl. Energy Mater.*, 2021, **4**, 10574–10583.

42 Z. Liu, J. Hu, H. Jiao, L. Li, G. Zheng, Y. Chen, Y. Huang, Q. Zhang, C. Shen, Q. Chen and H. Zhou, *Adv. Mater.*, 2017, **29**, 1606774.

43 Y. Liu, Z. Yang, D. Cui, X. Ren, J. Sun, X. Liu, J. Zhang, Q. Wei, H. Fan and F. Yu, *Adv. Mater.*, 2015, **27**, 5176–5183.

44 C. Xu, Z. Liu and E.-C. Lee, *J. Mater. Chem. C*, 2021, **9**, 679–686.

45 Z. Liu, L. Wang, X. Xie, C. Xu, J. Tang and W. Li, *Phys. Chem. Chem. Phys.*, 2022, **24**, 15912–15919.

46 Z. Liu, L. Wang, J. Han, F. Zeng, G. Liu and X. Xie, *Org. Electron.*, 2020, **78**, 105552.

47 G. Li, K. Chen, Y. Cui, Y. Zhang, Y. Tian, B. Tian, Y. Hao, Y. Wu and H. Zhang, *Adv. Opt. Mater.*, 2020, **8**, 1902012.